Phase transformations in substrate-free dissipative multistable metamaterials

Journal Article

Author(s):
Khajehtourian, Romik; Kochmann, Dennis M.

Publication date:
2020-05

Permanent link:
https://doi.org/https://doi.org/10.3929/ethz-b-000409286

Originally published in:
Extreme Mechanics Letters 37, https://doi.org/10.1016/j.eml.2020.100700

Extreme Mechanics Letters 37 (2020) 100700

Contents lists available at ScienceDirect

Extreme Mechanics Letters

journal homepage: www.elsevier.com/locate/eml

Phase transformations in substrate-free dissipative multistable metamaterials

Romik Khajehtourian, Dennis M. Kochmann *

Mechanics & Materials Lab, Department of Mechanical and Process Engineering, ETH Zürich, 8092 Zürich, Switzerland

ARTICLE INFO

Article history:
Received 26 January 2020
Received in revised form 29 March 2020
Accepted 29 March 2020
Available online 6 April 2020

Keywords:
Multistability
Metamaterial
Phase transformation
Reconfigurable structure
Transition wave

ABSTRACT

We show that propagating transitions fronts observed recently in multistable structural networks are analogous to solid–solid phase transformations in crystals and can therefore be described quantitatively as propagating shock fronts. We demonstrate that the well-established sharp-interface theory from shock physics agrees well with the exact and approximate wave solutions obtained from treating the multistable metamaterial as a discrete chain and as a homogenized continuum, respectively. We further discuss the energy transport that governs the underlying dynamic transition phenomenon. Through numerical examples we showcase the diverse nature of the achievable transition effects depending on the interplay between inertia and dissipation in the multistable network, which enables wave tailoring and guidance. We further confirm applicability of the theory by comparison to experimental data. Though focusing on one-dimensional transition front propagation as the most fundamental problem, our results and conclusions admit extension to higher dimensions.

1. Introduction

Propagating transition fronts describe a unique class of evolution events ubiquitous in physical systems, governing the kinetics of a wide range of structural transition phenomena — from dislocation motion to domain wall migration to shock waves in fluids and solids [1–6]. Equally found in biological [7] and chemical [8] systems, a non-convex, multi-welled potential energy landscape is the underlying cause that gives rise to multiple stable equilibrium states of the system, separated by energy barriers, and associated transition events that enable the system to locally switch between equilibrium states. Unlike in non-dissipative systems, where it is sufficient to establish a balance between nonlinearity and dispersion to form a soliton [9–11], dissipative systems require a balance between energy gains and losses for steady-state transition fronts [12]. These topological solitons, transition waves of constant speed, are an efficient means to carry changes within the system, transforming it locally from one stable equilibrium state to another, and propagating the boundary between domains of equal equilibrium states. If inertia is significant, propagating phase transformation fronts in solids are preceded by elastic shocks [13,14].

At the structural level, theoretical and experimental studies have mimicked such dynamic transition phenomena in mechanical analogs [15] with features reminiscent of the above material-level effects. In particular, transition waves of constant speed were demonstrated in bistable dissipative and diffusive one-dimensional (1D) chains [16–19] as well as in a two-dimensional (2D) system of coupled rotating units [20]. Although having been studied extensively theoretically (including an energy scaling law that governs the transition wave kinetics [17]), all of the aforementioned systems fell short of being true analogs of phase transformations in solids since each unit cell was grounded; i.e., each particle was attached to a discrete lattice, and the multistability entered through a non-convex, bistable *on-site* potential (as found, e.g., in the classical Frenkel–Kontrova (FK) model [21]). By contrast, most physical systems, including, e.g., phase transformations and deformation twinning, derive their multistability from a non-convex *interaction* potential without any grounding (so-called substrate-free). Mathematically speaking, in this latter case the non-convex potential does not depend on the primary fields of displacements, electric or magnetic fields but on their gradients. Recent experiments [22] presented an improved 2D structural analog of phase transformations based on a bistable interaction potential that admits dynamic snapping events from an open to a closed configuration (see Fig. 1 for a 1D chain of such bistable unit cells), stabilized by significant dissipation through material-intrinsic damping of the polymeric structural elements. Unfortunately, such transition phenomena at the structural level have not been investigated theoretically and raise questions about the underlying kinetics and energy transport — which is the subject of this study.

Of course, there is a rich body of literature on transition front propagation in discrete and continuous systems. Topological solitons [23,24] and solitary waves [25] were studied in discrete

* Corresponding author.
E-mail address: dmk@ethz.ch (D.M. Kochmann).

https://doi.org/10.1016/j.eml.2020.100700
2352-4316/

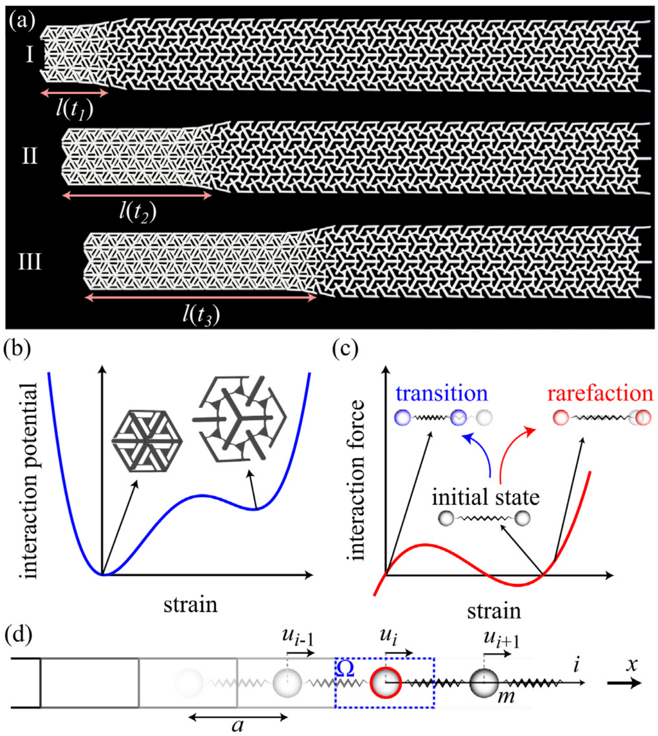

Fig. 1. (a) Snap shots of a transition wave propagating within a substrate-free bistable chain [22], illustrating the growing tail end of length $l(t)$. (b) The bistability stems from a double-well strain energy of each unit cell, whose minima correspond to the open and collapsed states. (c) The corresponding non-monotonous interaction force vs. strain curve illustrates how the initially stretched system, once impacted, displays a transition to the closed state (through a rarefaction wave that involves an unstable, stretched state). (d) Schematic of the physical model describing the effective mechanical behavior of the structure shown in (a) as a discrete chain of interacting particles of equal masses m in a periodic lattice arrangement spaced by distances a.

bistable non-dissipative systems along with conditions for the transition wave existence and kinetic relating their speed to the driving force [26]. A particular example, the well-known FK model is based on a multistable on-site potential [21], and variation of its on-site and interaction potentials covers a wide range of low-dimensional nonlinear physics problems such as the rupture of epitaxial films [27], the dynamics of a thin trapped layer between substrates [28], or arrays of Josephson junctions [29]. As a simplifying assumption, various works focused on chains of particles whose non-monotonic interaction forces (see Fig. 1c) were approximated by a piece-wise linear relation [5,6,30,31], which admits closed-form solutions of the system kinetics and was used to study, e.g., dispersion relations as well as subsonic and intersonic transition fronts. However, such approximations alter the system kinetics and, as in the present example of strongly nonlinear potentials, may alter the resulting transition behavior. Likewise, neglecting the dissipative nature of the system [32] alters the physics of the problem.

In continuous bodies, analogous to discrete systems, structural transformations due to non-convex multi-well potentials can also be classified into analogs of substrate-free and grounded categories [33], depending on whether the non-convex potential is on-site and hence depends on the primary field (e.g., on the electric or magnetic polarization in ferroelectrics and ferromagnetics, respectively) or on gradients of the primary field (such as on the strain field as in deformation twinning [34] or martensitic phase transformations [35,36], among others). Like in their structural analogs [22], those examples dissipate energy upon phase or domain boundary motion, and the propagating transition fronts have been described at the continuum scale by both sharp- and diffuse-interface models [37–39]. Again, the simplifying assumption of a piece-wise linear constitutive relation has enabled closed-form solutions of the kinetic relations and has also been applied to inhomogeneous solids with complex wave interactions [40].

This study is motivated by recent experiments performed on substrate-free 1D chains and 2D structures with multistable unit cell interactions; an example of such a 1D chain is shown in Fig. 1a. This structure was observed to produce stable, constant-speed transition waves [22] when friction with the ground is negligible. Even though experimental observations could be reproduced by a simple continuum model, the underlying kinetic relations and, in particular, the interplay between inertia and dissipation have not been explored. The latter is of particular interest as the nature of the response to impacting the system (thus triggering a propagating transition front) depends significantly on the relative importance of inertia (leading to ringing oscillations, producing a precursor rarefaction front, and leading to a conversion of stored potential energy into considerable kinetic energy) and dissipation (removing high-frequency oscillations, affecting the propagation speeds, and ultimately eliminating the rarefaction wave). The detrimental impact of friction in experiments further confirms the importance of rigid-body motion of the substrate-free metamaterial — in contrast to previous studies on grounded systems [17].

We here discuss the dynamics of a 1D multistable metamaterial from both a sharp-interface shock physics viewpoint and from a diffuse-interface solitary wave perspective, which provides insight into the system kinetics and connects the experimental scenario to well-established concepts within the phase transformation literature. Formulating the energy transport of transition waves as a balance between energy release and dissipation admits predicting the features of the propagating wave across the full range of inertia-dominated to dissipative/diffusive systems, including the recent experimental measurements. Beyond the motivating example of the 2D phase-transforming metamaterial in Fig. 1 [22], our findings extend to general discrete and continuous systems with bi- or multistable interaction potentials in the presence of dissipative mechanisms and can guide the structural design of nonlinear mechanical metamaterials.

2. Theoretical treatment of multistable structures

We consider a 1D periodic array of $N+1$ structural unit cells (Fig. 1a), each connected to its nearest neighbor unit cells and each having two stable equilibrium configurations (Fig. 1b). Applying a mathematical abstraction, the structure can be described as a 1D chain of $N+1$ particles (each representing a structural unit cell and carrying the mass m of the unit cell) connected by nonlinear interaction springs (Fig. 1d). When assuming that each unit cell is additionally subjected to friction with the ground and viscous drag due to a surrounding medium, Newton's second law of motion for the ith particle ($i = 0, \ldots, N$) becomes

$$m_i \ddot{u}_i + F_i^{\text{fr}} + \sum_{\alpha=i\pm1} \left(F_{i\alpha}^{\text{vis}} + F_{i\alpha}^{\text{nl}}\right) = 0, \quad (1)$$

in which $u_i(t)$ is the ith particle's displacement at time t (measured from its initial equilibrium position, so $u_i(0) = 0$), m_i is the particle mass, F_i^{fr} denotes a drag force (including both friction and viscous drag), and $F_{i\alpha}^{\text{vis}} = -F_{\alpha i}^{\text{vis}}$ and $F_{i\alpha}^{\text{nl}} = -F_{\alpha i}^{\text{nl}}$ are, respectively, viscous and nonlinear elastic interaction forces between particle i and its neighbors. Of course, several of those forces may not be present, depending on the particular system of interest, but we retain the above structure for generality; special cases will be deduced below. Here and in the following, dots denote time derivatives, while a comma in an index denotes a partial derivative with respect to the ensuing variable(s).

Unlike in grounded structures [17], we assume that the non-convexity of the system enters through the particle interactions, which we describe by a multi-welled interaction potential per length, $\psi(\varepsilon)$, such that

$$F_{i\alpha}^{\mathrm{nl}} = -\frac{\partial}{\partial u_i} a\psi(\varepsilon_{i\alpha}) = -\psi'(\varepsilon_{i\alpha}), \quad \varepsilon_{i\alpha} = \frac{u_\alpha - u_i}{a}, \tag{2}$$

with the relative distance change $\varepsilon_{i\alpha}$ depending on the particle displacements and the initially uniform particle distance a. This description is akin to phase transformations in solids (see, e.g., [35,41]), in which the free energy density depends on local strain measures.

Based on the observed strong damping due to intrinsic losses of the polymeric base material, we introduce the dissipative interaction forces $F_{i\alpha}^{\mathrm{vis}}$. As a leading-order approximation (and in line with [17–19]), we consider velocity-proportional damping with a constant viscosity $\beta \geq 0$. We thus assume that the viscous forces between particles derive from a convex viscous potential per length, $\phi(\dot{\varepsilon}_{i\alpha}) = \frac{\beta}{2}\dot{\varepsilon}_{i\alpha}^2$, which leads to

$$F_{i\alpha}^{\mathrm{vis}} = -\frac{\partial}{\partial \dot{u}_i} a\phi(\dot{\varepsilon}_{i\alpha}) = -\frac{\beta_{i\alpha}}{a}(\dot{u}_\alpha - \dot{u}_i). \tag{3}$$

Further considering dissipation through particle interactions with the surrounding environment — viz. through viscous drag when submerged in a medium, or through friction with the underlying surface (as observed in experiments [22]), the total force resisting the motion of the ith particle is written as

$$F_i^{\mathrm{fr}} = \gamma_i \dot{u}_i + \zeta_i \frac{\dot{u}_i}{|\dot{u}_i|} \tag{4}$$

with a velocity-proportional viscous damping coefficient $\gamma_i \geq 0$ and a dynamic friction coefficient $\zeta_i \geq 0$ (both depending on geometrical and material properties).

Altogether, the equation of motion for the ith particle ($i = 1, \ldots, N-1$) of the bistable chain reduces to

$$\begin{aligned} &m\ddot{u}_i + \gamma\dot{u}_i + \zeta\,\mathrm{sign}(\dot{u}_i) - \beta\frac{\dot{u}_{i+1} - 2\dot{u}_i + \dot{u}_{i-1}}{a} \\ &\quad - \psi'\left(\frac{u_{i+1} - u_i}{a}\right) + \psi'\left(\frac{u_i - u_{i-1}}{a}\right) = 0, \end{aligned} \tag{5}$$

while the analogous equations for the first and last particle depend on the boundary conditions. The experimental observation that fabrication-induced defects have no significant affect on transition waves justifies the assumption of uniform particle interactions, spacing, and material constants along the 1D chain (inviting the extension to more general settings in the future).

For chains with a sufficiently large number of particles and negligible discreteness effects, it will be convenient to work with a continuum approximation. To this end, we take $N \to \infty$ while keeping the total chain length $L = Na$ and the total mass $M = Nm$ unchanged. We assume that variations in the displacements are sufficiently smooth so we may write $u_i(t) = u(x_i, t)$ with $x_i = ia$ and a differentiable displacement field $u : [0, L] \times \mathbb{R} \to \mathbb{R}$. Inserting the latter into (5) and applying Taylor expansions, we obtain the approximation

$$\frac{m}{a}\ddot{u} + \frac{\gamma}{a}\dot{u} + \frac{\zeta}{a}\mathrm{sign}(\dot{u}) - \beta\dot{u}_{,xx} - \psi''(u_{,x})u_{,xx} + O(a) = 0. \tag{6}$$

With the mass density $\rho = m/a = M/L$, viscosity $\eta = \gamma/a$ and friction $\tau = \zeta/a$ per length, and assuming that $m, \gamma, \zeta \sim O(a)$ and $\beta, \psi \sim O(1)$ (which is reasonable for mass and energy conservation), the limit $N \to \infty$ (or $a \to 0$) yields the continuum law of linear momentum balance for the 1D chain:

$$\rho\ddot{u} + \eta\dot{u} + \tau\,\mathrm{sign}(\dot{u}) - \beta\dot{u}_{,xx} - \psi''(u_{,x})u_{,xx} = 0. \tag{7}$$

3. Transition waves

Among the possible solutions of (5) and (7) we are primarily interested in those that represent transition waves, i.e., constant-speed transition fronts with a steady-state profile (in other words, topological solitons). There may surely exist other solutions such as linear waves and envelope solitons, yet those generally decay in dissipative and diffusive systems, whereas transition waves – traveling over long distances within the chain – are of interest for applications and were demonstrated experimentally [22].

We assume the chain of Fig. 1d, described by the above equation of motion, is initially at rest in a stable, uniformly stretched equilibrium state with equal inter-particle strains ε_s so $\psi'(\varepsilon_s) = 0$ (see Fig. 2). Once initiated, e.g., by impacting the first particle, the chain is successively transformed by switching the distance between each pair of particles from the stretched stable equilibrium distance $(1 + \varepsilon_s)a$ to an energetically lower stable distance $(1 + \varepsilon_0)a$ characterized by inter-particle strains $\varepsilon_s > 0$ and $\varepsilon_0 = 0$. If the chain is sufficiently long, steady-state waves can fully establish before reflections from the chain end start to play a role (we hence neglect reflections and, in all examples, assume $u_N(t) = u(L, t) = 0$ without loss of generality).

When impacted, the 1D multistable medium may produce two kinds of wave fronts (see Fig. 2). A *phase transition front* (or kink), propagating at speed V, transforms the state of the system from one phase to another, hence jumping from one well of the non-convex potential ψ to the other (analogous to the discrete case shown in Fig. 1c). Such a transition front alone (switching the system directly from the high- to the low-energy equilibrium) is energetically unfavorable [13,14]. Instead, a *rarefaction front* (or shock) propagates at speed C as a precursor to the transition front. Such rarefaction shock fronts have been observed in continuous solids (e.g., in elastic bars [13]) and their existence conditions derived within continuum mechanics and solid-state physics [14,42]. As schematically shown in Fig. 2, the rarefaction front separates regions of strain states within the same phase, i.e., the interactions ahead of and behind the front lie within the same well of ψ.

Such propagating wave fronts are traditionally described by either sharp- or diffuse-interface models. Presuming that the transition front is sufficiently smooth and localized, both admit the same conclusions. Here, we briefly discuss both approaches to establish the kinetic wave transport relations and to derive the resulting wave profiles (for discrete and continuous systems).

3.1. Sharp interfaces: shock description

Following a sharp-interface model [37], we describe a propagating front as a translating discontinuity within an otherwise continuous displacement field $u(x, t)$ and associated strains $\varepsilon = u_{,x}$. We define the jump of a field p across the front as $[\![p]\!] = (p_+ - p_-)$, in which p_+ and p_- denote the values of p ahead and behind the front, respectively. Likewise, the average value is denoted by $\langle p \rangle = (p_+ + p_-)/2$.

Kinematic compatibility across a wave front moving at speed v requires $[\![\dot{u}]\!] + v[\![\varepsilon]\!] = 0$, while linear momentum balance across the interface enforces $[\![\psi']\!] + \rho v[\![\dot{u}]\!] = 0$, where we only consider the rate-independent stresses (dissipative effects will be considered below). Together, these jump conditions imply that $[\![\psi']\!] = \rho v^2[\![\varepsilon]\!]$. This confirms that a direct transition from ε_s to ε_0 (i.e., from state 1 to 3 in Fig. 2) is impossible, since $\psi'(\varepsilon_0) = \psi'(\varepsilon_s) = 0$ would imply a zero propagation velocity v. Instead, the system transitions first to an intermediate state 2 with strain $\varepsilon_r \geq \varepsilon_s$, and from there to 3 with strain ε_0. This produces the combination of rarefaction and transition fronts (or

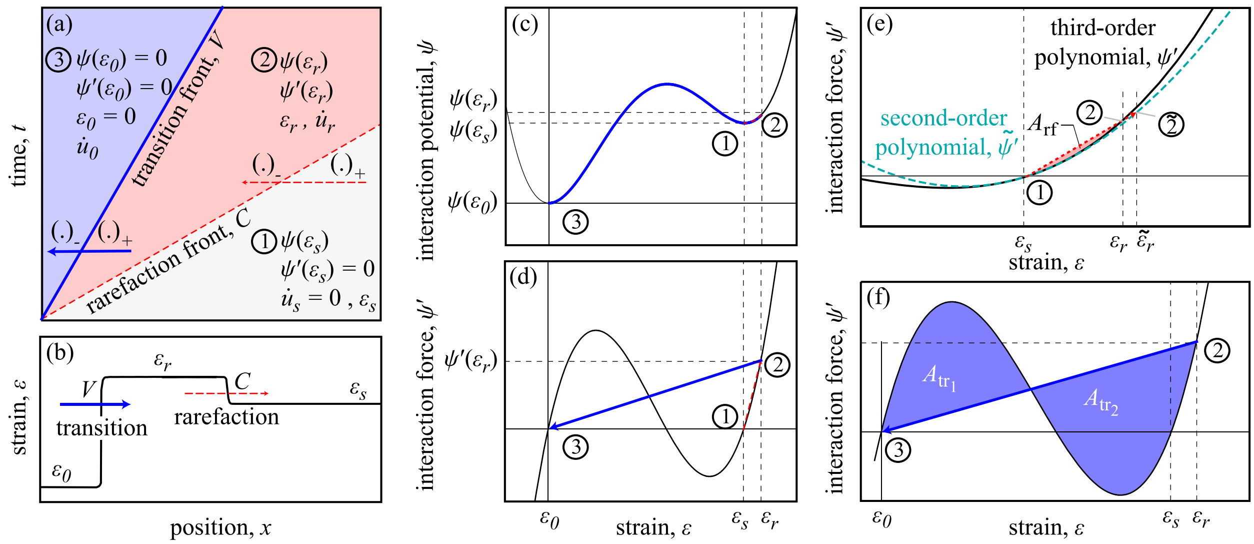

Fig. 2. Admissible solution to (5) and (7) for $\gamma = \zeta = 0$. (a) Rarefaction (intersonic) and transition (subsonic) fronts with velocities C and V, respectively, separate regions 1, 2, and 3 with the indicated strains, particle velocities, interaction potentials, and interaction forces. (b) Strain profile with transition and rarefaction fronts. (c) A typical bistable interaction potential $\psi(\varepsilon)$, (d) resulting interaction force (stress) $\psi'(\varepsilon)$. (e) Second-order approximation of the interaction force (stress) around ε_s. Rarefaction path changing the state of the structure from 1 to 2 (or $\tilde{2}$) is shown for third-order (or second-order) polynomial by red dotted line. The shaded area A_{rf} represents the driving force of the rarefaction front. (f) The difference between the shaded areas ($A_{\mathrm{tr}_1} - A_{\mathrm{tr}_2}$) represents the driving force of the transition front.

shocks and kinks [13,14]) shown in Fig. 2a (unless inertial effects are negligible).

Applying the above relations to the rarefaction front with speed $v = C$, separating regions 1 and 2 in Fig. 2a), we find the driving force on the shock (the colored area A_{rf} in Fig. 2e) as

$$f_{\mathrm{rf}} = \psi(\varepsilon_s) - \psi(\varepsilon_r) + \frac{\rho C^2}{2}(\varepsilon_s - \varepsilon_r)^2 = \psi(\varepsilon_s) - \psi(\varepsilon_r) + \frac{\rho \dot{u}_r^2}{2}. \quad (8)$$

Analogously, for the transition front with speed $v = V$ separating regions 2 and 3 the driving force f_{tr} (i.e., the difference $A_{\mathrm{tr}_2} - A_{\mathrm{tr}_1}$ in the colored areas of Fig. 2f) is

$$f_{\mathrm{tr}} = \psi(\varepsilon_r) - \frac{\rho V^2}{2}\varepsilon_r^2 = \psi(\varepsilon_r) - \frac{\rho\,(\dot{u}_r - \dot{u}_0)^2}{2}. \quad (9)$$

We emphasize that both waves are dissipative, unlike in the classical trilinear stress–strain assumption [40], where the stress–strain branch for the rarefaction wave is linear (thus entailing zero dissipation). The second law of thermodynamics dictates $f_{\mathrm{rf}} C \geq 0$ and $f_{\mathrm{tr}} V \geq 0$. From (8) we see that $f_{\mathrm{rf}} > 0$ and hence $C \geq 0$ as long as $0 \leq \psi''(\varepsilon_s) < \psi''(\varepsilon_r)$. Likewise, (9) requires $\psi(\varepsilon_r) > \psi'(\varepsilon_r)\varepsilon_r/2$ for $f_{\mathrm{tr}} > 0$ and hence $V \geq 0$. If both conditions are met, both waves propagate in the positive direction.

We note that, while the potential $\psi(\varepsilon)$, density ρ, strains $\varepsilon_0 = 0$ and $\varepsilon_s > 0$, and particle velocity $\dot{u}_s = 0$ are known for a given multistable network, the particle velocities $\dot{u}_r$, $\dot{u}_0$, propagation speeds C and V, and strain ε_r are unknown a priori. Hence, we have five unknowns for four jump conditions (displacement and traction compatibility across each propagating front), which leads to a family of solutions. In the special case of $\beta = 0$ (no dissipation due to particle interactions), (8) and (9) provide the additional (dependent) equations

$$\psi(\varepsilon_r) = \frac{\rho V^2}{2}\varepsilon_r^2, \qquad \psi'(\varepsilon_r) = \frac{2\big(\psi(\varepsilon_s) - \psi(\varepsilon_r)\big)}{\varepsilon_s - \varepsilon_r}, \quad (10)$$

from which one may solve the system uniquely (we will discuss transition wave solutions for this special case in Section 4.2). However, for the general case $\beta > 0$, no analytical solution is feasible. Since the shape of the wave front affects the dissipation, a kinetic relation (involving the driving force, the viscous damping, and the transition velocities for given potentials and material constants) requires solving for the traveling wave profile with its diffuse interface. Of course, we acknowledge that the above treatment is only a sharp-interface approximation of a truly discrete phenomenon with unique wave front profiles depending on the system parameters (here, the unit cell architecture and resulting energy landscape, the mass distribution, and the dissipative mechanisms).

3.2. Diffuse interfaces: energy transport in a discrete chain

For either transition or rarefaction wave, we assume that the discrete 1D chain governed by (5) admits a sufficiently smooth traveling wave solution with a constant propagation speed $v \in \mathbb{R}$ such that $u_i(t) = \hat{u}(\xi) + ia\varepsilon_{int}$ where $\xi = ia - vt$, and ε_{int} denotes the initial uniform strain between particles. For the rarefaction wave we have $\varepsilon_{int} = \varepsilon_s$ and $v = C$, while for the transition wave $\varepsilon_{int} = \varepsilon_r$ (with some unknown strain ε_r) and $v = V$. In the following, we keep the derivation general and apply the specific cases of rarefaction and transition waves only once the energy transport relations have been derived.

We multiply the equation of motion (5) for the ith particle by $u_{,\xi}$ and integrate over the whole chain ($0 \leq x \leq L$ with $x = ia$, or, equivalently, $-vt \leq \xi \leq L - vt$, assuming $0 < |vt| < L$ for a well-established wave), which leads to

$$\begin{aligned} &\int_{-vt}^{L-vt} m v^2 u_{,\xi\xi} u_{,\xi} d\xi - \int_{-vt}^{L-vt} \gamma v u_{,\xi}^2 \,\mathrm{d}\xi + \int_{-vt}^{L-vt} \zeta u_{,\xi} \,\mathrm{d}\xi \\ &+ \int_{-vt}^{L-vt} \beta v \frac{u_{,\xi}(\xi + a) - 2u_{,\xi}(\xi) + u_{,\xi}(\xi - a)}{a} u_{,\xi} \,\mathrm{d}\xi \\ &- \int_{-vt}^{L-vt} \psi'\left(\frac{u(\xi + a) - u(\xi)}{a}\right) u_{,\xi} \,\mathrm{d}\xi \\ &+ \int_{-vt}^{L-vt} \psi'\left(\frac{u(\xi) - u(\xi - a)}{a}\right) u_{,\xi} \,\mathrm{d}\xi = 0. \end{aligned} \quad (11)$$

Here, we assume $v > 0$ (i.e., the wave travels from left to right) without loss of generality (the opposite case can easily concluded), and examine the individual integrals, inspired by the grounded-chain analysis in [17]. Note that the situation here is fundamentally different, since the tail end of the chain is moving with constant $v \neq 0$ (unlike in the grounded case where the tail end is at rest), and our chain is of finite length.

We exploit the expected solution of a topological soliton (i.e., constant strains and velocities far away from the wave front on both sides) to successively transform each of the integral terms in (11); details are summarized in Appendix A. Starting with the inertial term, the topological soliton simplifies the first integral in (11) to

$$\int_{-vt}^{L-vt} mv^2 u_{,\xi\xi} u_{,\xi} \,\mathrm{d}\xi = \frac{m}{2}[\![\dot{u}^2]\!], \tag{12}$$

in which $\dot{u}_+$ and $\dot{u}_-$ are, respectively, the particle velocities ahead and behind the traveling wave (Fig. 2a), and we abuse our definition $[\![\cdot]\!]$ for the difference of a field far ahead of and behind the wave front.

The integral associated with viscous drag in (11) becomes

$$-\int_{-vt}^{L-vt} \gamma v {u_{,\xi}}^2 \,\mathrm{d}\xi \approx -\frac{\gamma}{v}[\![\dot{u}^2]\!]\, l(t), \tag{13}$$

where we exploit that the particles ahead of the wave front are at rest, so the integral involves only those particles included in the tail end of the chain moving at constant speed v. Therefore, $l(t)$ represents an effective length of the tail behind the front at time t (neglecting those few particles close to the transition front having different speeds); if $N \gg 1$, then $l(t) = vt$. The growing tail end moving at constant speed is shown in the experimental snapshots of Fig. 1a at three different times t. Analogously, the friction term in (11) becomes $-\zeta[\![\dot{u}]\!]\, l(t)/v$.

The interaction dissipation integral in (11) turns into

$$\begin{aligned} &\int_{-vt}^{L-vt} \beta v \frac{u_{,\xi}(\xi-a) - 2u_{,\xi}(\xi) + u_{,\xi}(\xi+a)}{a} u_{,\xi}\,\mathrm{d}\xi \\ &\approx -\frac{aD_{\mathrm{discr}}}{v}, \quad D_{\mathrm{discr}} = 2\int_0^L \phi(\dot{\varepsilon})\,\mathrm{d}x \approx 2\sum_{i=1}^{N-1}\phi(\dot{\varepsilon}_i)a \end{aligned} \tag{14}$$

where D_{discr} represents the total dissipation due to the viscous particle interactions in the discrete chain.

Finally, the integral involving the non-convex interaction potential in (11) yields

$$\begin{aligned} -\int_{-vt}^{L-vt} &\left[\psi'\left(\frac{u(\xi+a)-u(\xi)}{a}\right)\right. \\ &\left.\quad -\psi'\left(\frac{u(\xi)-u(\xi-a)}{a}\right)\right] u_{,\xi}\,\mathrm{d}\xi \\ &= a\int_{\varepsilon_-}^{\varepsilon_+} \psi'(\varepsilon)\,\mathrm{d}\varepsilon = a[\![\psi]\!], \end{aligned} \tag{15}$$

where we exploited that the wave separates regions of constant strains $\varepsilon_\pm$.

Combining (12)–(15) and the frictional term, we obtain the energy transport balance in the dissipative discrete chain of particles as

$$\frac{m}{2}[\![\dot{u}^2]\!] + a[\![\psi]\!] \approx \frac{aD_d}{v} + (2\gamma\langle\dot{u}\rangle + \zeta)\frac{[\![\dot{u}]\!]}{v} l(t). \tag{16}$$

In words, the change in kinetic plus potential energy is accommodated by dissipation consisting of inter-particle viscous dissipation, drag, and friction.

Notice that the last term (the combined effects of friction and viscous drag) is the only time-dependent term in (16) due to the growing, moving tail of length $l(t) \approx vt$, while the portion of the structure ahead of the transition front remains approximately at rest. Any friction or drag forces hence increase over time due to the growing tail end, so that a steady-state solution with $v =$ const. can only exist (and hence (16) can hold) if $2\gamma\langle\dot{u}\rangle + \zeta = 0$, which in turn – considering the second law of thermodynamics – requires that there be *no friction nor viscous drag*. This is in fact intuitive: including friction or drag must necessarily slow down a transition front, as the energy losses due to friction and drag grow over time through the growing tail. This explains why experiments [22] observed stable transition waves only if friction with the ground was negligible. A possible avenue to achieve constant wave speeds in the presence of friction (or drag) is a geometrically graded chain, in which the energy release per transition event $[\![\psi(\varepsilon)]\!]$ increases along the chain.

In the absence of friction and viscous drag, a steady transition wave of constant speed exists for a uniform potential difference $[\![\psi]\!]$, as seen in experiments [22]. In this case, (16) simplifies to (after division by a and using $\rho = m/a$)

$$\frac{D_{\mathrm{discr}}}{v} \approx [\![\psi]\!] + \frac{\rho}{2}[\![\dot{u}^2]\!]. \tag{17}$$

Recall that this relation holds approximately, since we assumed a smooth wave profile and sufficiently wide transition front, so the total dissipation D_{discr} is approximated by an integral instead of a discrete sum over all particles.

As shown in Fig. 2a, we consider two wave fronts propagating in the chain. The *rarefaction front* changes the strain between particles from the initial ε_s to an intermediate ε_r. By shifting particle velocities to the moving front's reference frame accordingly to obtain $v = C$, we turn (17) into

$$\frac{D^{\mathrm{rf}}_{\mathrm{discr}}}{C} \approx \psi(\varepsilon_s) - \psi(\varepsilon_r) + \rho\frac{\dot{u}_r^2}{2}, \tag{18}$$

whose dissipation $D^{\mathrm{rf}}_{\mathrm{discr}}$ is localized in the rarefaction front.

The *transition wave*, by contrast, switches the strain of each particle interaction from the intermediate ε_r to the low-energy equilibrium strain ε_0. Analogous to the rarefaction front, we shift the particle velocities to ensure $v = V$. Hence, for a subsonic front (17) becomes

$$\frac{D^{\mathrm{tr}}_{\mathrm{discr}}}{V} \approx \psi(\varepsilon_r) - \psi(\varepsilon_0) - \rho\frac{(\dot{u}_0 - \dot{u}_r)^2}{2}, \tag{19}$$

where $D^{\mathrm{tr}}_{\mathrm{discr}}$ is the dissipation localized around the transition front. As expected, (18) and (19) are in agreement with their sharp-interface counterparts (8) and (9), respectively, when $D^{\mathrm{rf}}_{\mathrm{discr}} = f_{\mathrm{rf}}C$ and $D^{\mathrm{tr}}_{\mathrm{discr}} = f_{\mathrm{tr}}V$.

Note that the solution of a propagating front with $V, C > 0$ only holds when the phase transformation switches the system from an energetically higher to an adjacent lower equilibrium, i.e., $\Delta\psi > 0$, independent of the topology of the interaction potential. By contrast, if $\Delta\psi < 0$, then no such solution exists, which produces the behavior typical of a mechanical diode [18]. Note that (17) also holds in the massless limit ($\rho \to 0$), where it recovers the original scaling law for grounded systems [17]. Further, it was shown for grounded systems [16] that a steady-state solution exists in the dissipation-free case ($D = 0$) if $\Delta\psi = 0$ (equal energy wells). Here, this still applies in the massless limit. In the presence of inertial effects, an energy release $\Delta\psi > 0$ is required even in the dissipation-free limit, since the kinetic energy must be balanced. We add that the dissipation-free case is generally problematic here, since the complete transfer of potential into kinetic energy, following (17), produces considerable twinkling modes that may ultimately corrupt the transition front motion and cause chaotic motion.

The nonlinear energy transport relation does not admit superposition of multiple double-well transitions — unlike for grounded systems where the superposition of double-well transitions for both dissipative and diffusive systems holds [17]. Here, linear superposition does not apply for transitions farther than between adjacent stable states (unless in the massless limit where relations become linear).

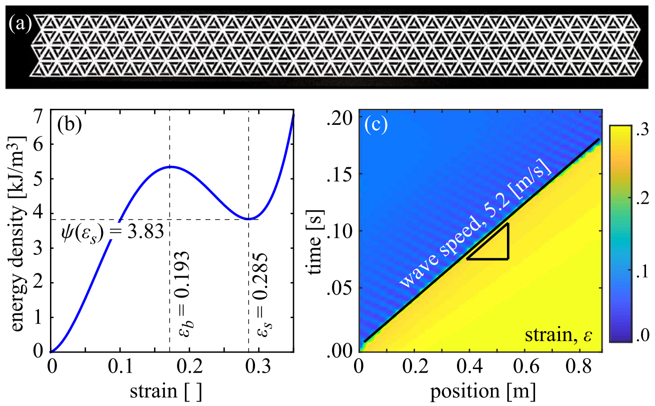

Fig. 3. (a) Substrate-free 1D tessellation consisting of 32 × 2 unit cells. (b) Energy density vs. volumetric expansion strain (quartic polynomial (21) fitted to the experimental data of [22]). (c) Spatiotemporal diagram of the simulated discrete chain motion overlaid with the experimentally measured wave speed from [22].

Finally, in the limit of a negligible rarefaction front (i.e., $\varepsilon_r \to \varepsilon_s$), we have $f_{\mathrm{rf}} = 0$ and $\dot{u}_r = \dot{u}_s = 0$, so

$$\frac{D^{\mathrm{tr}}_{\mathrm{discr}}}{V} + \rho\frac{\dot{u}_0^2}{2} \approx \Delta\psi. \tag{20}$$

This shows that the excess energy released by the transition event is consumed by both viscous interactions and the kinetic energy of the chain's tail.

As one may expect, the above procedure of taking the discrete equations of motion and applying a continuous displacement field yields (approximately) the same energy exchange as when starting with a continuum governing equation based on (7) (see Appendix B).

4. Bistable metamaterials

The structure shown in Fig. 1 is derived from unit cells that are bistable when periodically tessellated, as shown experimentally in [22]. It was shown that the non-convex interaction potential of those structures (determined experimentally and computed by finite elements, see Fig. 3(b)) is described well by a quartic polynomial

$$\psi(\varepsilon) = c_2\varepsilon^2 + c_3\varepsilon^3 + c_4\varepsilon^4. \tag{21}$$

Such quartic potentials are classical in martensitic phase transformations [41,43] and ferroelectrics/-magnetics in 2D [44]. Assuming that the above quartic potential has two stable equilibria at $\varepsilon_0 = 0$ and $\varepsilon_s > 0$ with a potential difference of $\Delta\psi = \psi(\varepsilon_s) - \psi(\varepsilon_0)$, we identify the coefficients as

$$c_3 = -\frac{2\varepsilon_s^2 - 4\Delta\psi_0}{\varepsilon_s^3}c_2, \qquad c_4 = \frac{\varepsilon_s^2 - 3\Delta\psi_0}{\varepsilon_s^4}c_2, \tag{22}$$

with the rescaled energy difference $\Delta\psi_0 = \Delta\psi/c_2$ and

$$c_2 > 0 \quad \text{and} \quad \varepsilon_s > \sqrt{6\Delta\psi_0}. \tag{23}$$

The two stable equilibria are separated by an unstable equilibrium defined by

$$\varepsilon_b = \frac{\varepsilon_s^3}{2(\varepsilon_s^2 - 3\Delta\psi_0)}, \quad \psi(\varepsilon_b) = \frac{\varepsilon_s^6(\varepsilon_s^2 - 4\Delta\psi_0)}{16(\varepsilon_s^2 - 3\Delta\psi_0)}c_2, \tag{24}$$

with a total energy barrier $\psi(\varepsilon_b)$. In the special case of $\Delta\psi = 0$, the double-well potential becomes symmetric (as in the grounded case of [16]).

4.1. Rarefaction front profile

For the double-well interaction potential (21) (and neglecting friction and drag to enable a steady-state solution), linear momentum balance (7) admits an analytical solution. To obtain the elastic wave profile we write (7) as

$$\rho\ddot{u} - \beta\dot{u}_{,xx} - \left[\tilde{\psi}'(u_{,x})\right]_{,x} = 0, \tag{25}$$

in which we use the harmonic approximation (see Fig. 2e)

$$\tilde{\psi}'(u_{,x}) = d_1(u_{,x} - \varepsilon_s) + d_2(u_{,x} - \varepsilon_s)^2 + \text{h.o.t.} \tag{26}$$

with

$$d_1 = \frac{2\varepsilon_s^2 - 12\Delta\psi_0}{\varepsilon_s^2}c_2, \quad d_2 = \frac{6\varepsilon_s^2 - 24\Delta\psi_0}{\varepsilon_s^3}c_2, \tag{27}$$

since the rarefaction front leaves the chain in the same energy well. Substitution of the traveling-wave solution $u(x,t) = \hat{u}(\xi) + \varepsilon_s x$ with $\xi = x - Ct$ into (25) results in

$$\rho C^2\hat{u}_{,\xi\xi} + \beta C\hat{u}_{,\xi\xi\xi} - d_1\hat{u}_{,\xi\xi} - 2d_2\hat{u}_{,\xi}\hat{u}_{,\xi\xi} = 0, \tag{28}$$

which has the blow-up solution (with integration constants Γ_1, Γ_2, $\Gamma_3 \in \mathbb{R}$)

$$\begin{aligned}\hat{u}(\xi) = {} & \Gamma_3 - \frac{d_1\xi}{2d_2} + \frac{\rho C^2\xi}{2d_2} \\ & - \frac{C\beta}{d_2}\ln\left[\cos\frac{(\xi + \Gamma_2)\sqrt{4d_2C\beta\Gamma_1 - (d_1 - \rho C^2)^2}}{2C\beta}\right].\end{aligned} \tag{29}$$

The strain profile $\varepsilon(\xi) = \hat{u}_{,\xi}(\xi) + \varepsilon_s$ follows from (29) by setting $\Gamma_1 = \Gamma_2 = 0$ to keep the solution bounded:

$$\varepsilon(\xi) = \varepsilon_s - \frac{d_1 - \rho C^2}{2d_2}\left[1 + \tanh\frac{\xi(d_1 - \rho C^2)}{2C\beta}\right]. \tag{30}$$

4.2. Transition front profile

Modeling the transition front requires us to consider the exact nonlinear potential $\psi(\varepsilon)$ (instead of the above harmonic approximation), for which differentiating (7) with respect to x (assuming $\eta = 0$ and $\tau = 0$), substituting a traveling-wave solution $\varepsilon(x,t) = \hat{\varepsilon}(\xi) + \varepsilon_s$, and integrating twice results in (with $\Gamma_1, \Gamma_2 \in \mathbb{R}$)

$$\rho V^2\varepsilon + \beta V\varepsilon_{,\xi} - \psi'(\varepsilon) + \Gamma_1\xi + \Gamma_2 = 0. \tag{31}$$

For a continuous 1D medium in which a transition front of constant speed V propagates from left to right, both far-ends of the body experience uniform strains in an equilibrium state (i.e., $\varepsilon_{,\xi} = 0$ and $\psi'(\varepsilon) = 0$ when $|\xi| \gg 0$). Specifically, the left-end tail is at $\varepsilon = \varepsilon_0 = 0$ and moving with V, while the right end of the body is at $\varepsilon = \varepsilon_s > 0$. Consequently, we must have $\Gamma_1 = \Gamma_2 = 0$, so that (31) reduces to (with $\beta > 0$)

$$\varepsilon_{,\xi} = \frac{1}{\beta V}\left[\psi'(\varepsilon) - \rho V^2\varepsilon\right]. \tag{32}$$

This is an autonomous ordinary differential equation. Substituting the double-well potential (21) into (32) gives

$$\begin{aligned}\xi = -\frac{V\beta}{4c_2 - 2V^2\rho}\Bigg[& \frac{6c_3}{\sqrt{-9c_3^2 + 32c_2c_4 - 16c_4V^2\rho}} \\ & \arctan\left(\frac{3c_3 + 8c_4\varepsilon}{\sqrt{-9c_3^2 + 32c_2c_4 - 16c_4V^2\rho}}\right) \\ & -2\ln\varepsilon + \ln\left(2c_2 + 3c_3\varepsilon + 4c_4\varepsilon^2 - V^2\rho\right)\Bigg]_{\varepsilon=\varepsilon_{\mathrm{int}}}^{\varepsilon=\varepsilon(\xi)},\end{aligned} \tag{33}$$

which can be solved numerically for the equilibrium solution $\varepsilon_\xi(\xi)$ of (32) with an initial strain ε_{int}, when assuming a propagating transition front in an infinite medium (i.e., neglecting end effects). The solution describes the profile of the transition wave from its deformed state with strain ε_r to the undeformed equilibrium state with strain ε_0. In the limit of $\xi \to \pm\infty$ solutions are respectively constant values ε_r and ε_0, corresponding to 2 and 3 in Fig. 2c.

We close by relating the problem studied here to classical nonlinear dynamics solutions. Substituting the quartic potential (21) into the discrete equation of motion (5) (with $\gamma = 0$ and $\zeta = 0$) and applying fourth-order Taylor expansions gives

$$\begin{aligned} m\ddot{u} &- \beta a\dot{u}_{,xx} - \beta\frac{a^3}{12}\dot{u}_{,xxxx} - 2ac_2u_{,xx} \\ &- 6ac_3u_{,x}u_{,xx} - 12ac_4u_{,x}^2u_{,xx} - \frac{a^3}{6}c_2u_{,xxxx} \\ &- a^3c_4u_{,xx}^3 - a^3c_3u_{,xx}u_{,xxx} - 4a^3c_4u_{,x}u_{,xx}u_{,xxx} \\ &- \frac{a^3}{2}c_3u_{,x}u_{,xxxx} - a^3c_4u_{,x}^2u_{,xxxx} + O(a^5) = 0. \end{aligned} \tag{34}$$

By dropping all terms containing derivatives of fifth order and higher as well as all those terms whose combined derivatives add up to fifth order (i.e., all terms containing $\prod_i (u^{(p_i)})^{q_i}$ with $\sum_i p_iq_i \geq 5$) in (34), differentiating with respect to x, substituting the traveling wave solution $\varepsilon(x,t) = \hat{\varepsilon}(\xi) + \varepsilon_r$, and integrating twice, we arrive at the damped Helmholtz–Duffing equation,

$$\begin{aligned} \frac{c_2a^2}{6}\hat{\varepsilon}_{,\xi\xi} - \beta v\hat{\varepsilon}_{,\xi} + \left[\psi''(\varepsilon_r) - \rho v^2\right]\hat{\varepsilon} \\ + \frac{\psi'''(\varepsilon_r)}{2}\hat{\varepsilon}^2 + \frac{\psi''''(\varepsilon_r)}{6}\hat{\varepsilon}^3 = 0, \end{aligned} \tag{35}$$

in which the integration constants were set to zero. In the limit $\beta \to 0$ (vanishing dissipation), (35) becomes a nonlinear Klein–Gordon equation which is solvable analytically [45]; unfortunately, no such solution exists for the general damped case. Therefore, numerical results are presented below.

5. Results

To verify the above derivations and demonstrate specific examples of traveling wave front solutions in 1D arrangements of bistable structural unit cells, we non-dimensionalize the discrete equation of motion (5) by assuming $\gamma = \zeta = 0$ and defining $\bar{u} = u/a$ and $\bar{t} = t/T$ so that

$$\begin{aligned} \bar{\rho}\bar{u}_{i,\bar{t}\bar{t}} - \bar{\beta}\left(\bar{u}_{i+1,\bar{t}} - 2\bar{u}_{i,\bar{t}} + \bar{u}_{i-1,\bar{t}}\right) \\ - \bar{\psi}'\left(\bar{u}_{i+1} - \bar{u}_i\right) + \bar{\psi}'\left(\bar{u}_i - \bar{u}_{i-1}\right) = 0, \end{aligned} \tag{36}$$

with dimensionless parameters $\bar{\rho} = ma/T^2f_0$ and $\bar{\beta} = \beta/Tf_0$ with $f_0 = \psi'/\bar{\psi}'$, and overbars being omitted in the following for simplicity. Inspired by experiments [22], we consider a chain initially at rest, stretched to the equilibrium strain $\varepsilon_s > 0$. The first particle from the left is subjected to an impact imposed as an initial velocity v_{imp} at $t = 0$, which is sufficiently large to transform the first particle interaction from ε_s to $\varepsilon_0 = 0$.

5.1. Experimental transition waves

The sample Fig. 3a consists of 32 × 2 unit cells and is made of a thermoplastic acetal homopolymer resin [22]. The non-convex interaction energy density was determined through uniaxial tensile and compression tests and reproduced by finite element simulations. In particular the latter numerical approach allows one to, in principle, obtain $\psi(\varepsilon)$ for various unit cell geometries and base materials in experiments. As shown in [22], the particular structure Fig. 3a was characterized by a non-convex potential ψ that was well approximated by a quartic polynomial as in (21) (reproduced in Fig. 3b). As predicted by theory and observed in experiments, a transition front of constant speed forms. Based on the above theory, we use the measured wave speed $V = 5.2$ m/s and the energy density from Fig. 3b to calculate the viscosity constant β, based on which we reproduce the experimental result by simulating this structure, solving (36) numerically. The results, shown in Fig. 3c, yield the observed constant-speed transition front. Notice that due to the low mass density in experiments, only a transition front was visible in experiments while the rarefaction front was not distinguishable. We point out that the chosen quadratic dissipation potential (characterized by a single, scalar damping constant β) is a relatively simple choice and hence to be viewed as a first-order approximation. In reality, the dissipation depends on the distribution of strain rates across a deforming unit cell and can therefore be linked to the geometry of the unit cell, analogous to the elastic interaction potential. Based on the agreement between simulations and experimental data we here do not investigate this relation further, whereas detailed experiments or simulations can indeed shed light on the relation between a unit cell architecture and the resulting viscous dissipation potential.

5.2. Exploring the design space

We precede to present numerical results for various bistable chains with different mass densities as well as potential energy landscapes (corresponding to variations in unit cell geometry and base materials) to explore the rich space of achievable waves through to the competition of inertia and dissipation. Throughout, we consider $\gamma = 0$, $\zeta = 0$ (no friction and drag). In all simulations, the exact boundary condition at the rightmost particle is irrelevant, as we assume a long chain without end effects. Unless otherwise defined, we use the interaction potential from (21) with $\Delta\psi_0 = 0.01$, $\varepsilon_s = 0.25$, and $c_2 = 100$.

Upon impact and establishment of a transition, we generally observe the formation of two fronts of constant velocities (an example is shown in Fig. 4). Differentiating the displacement solution in space, results in the strain field solution (Fig. 4b) which, together with the particle velocity field (Fig. 4c), provides all necessary information about the three regions introduced in Fig. 2. In addition, we obtain the strain and particle velocity profiles shown in Figs. 4d and 4e at four different times $t_i > 0$. Note that these results are for significant damping ($\beta = 0.25$, $m = 0.01$), so a steady-state wave establishes with decaying twinkling modes. The strong dissipative effects are also responsible for the wave velocities being nearly unaffected by the initial impulse (see Appendix C). For all practical purposes the characteristics of the propagating fronts are hence dictated by the geometric and material properties of the chain, and we regard them as independent of the initial conditions in the following.

To understand the effect of the precursor shock on the phase transition, we find the rarefaction strain ε_r as a function of V. For the interaction potential (21), we solve $\psi'(\varepsilon_r) = \rho V^2\varepsilon_r$ for its three roots, viz. $\varepsilon_r = 0$ and

$$\varepsilon_r = \frac{-3c_3 \pm \sqrt{9c_3^2 + 16(\rho V^2 - 2c_2)c_4}}{8c_4}, \tag{37}$$

among which only the positive one is physically meaningful. The curves in Fig. 5 demonstrate the positive normalized root for various values of ρ and β. Comparison with the results of numerical discrete-chain simulations reveals excellent agreement for all cases tested. Results further indicate that the effect of the rarefaction wave decreases in the diffusive limit; i.e., $\rho \to 0$

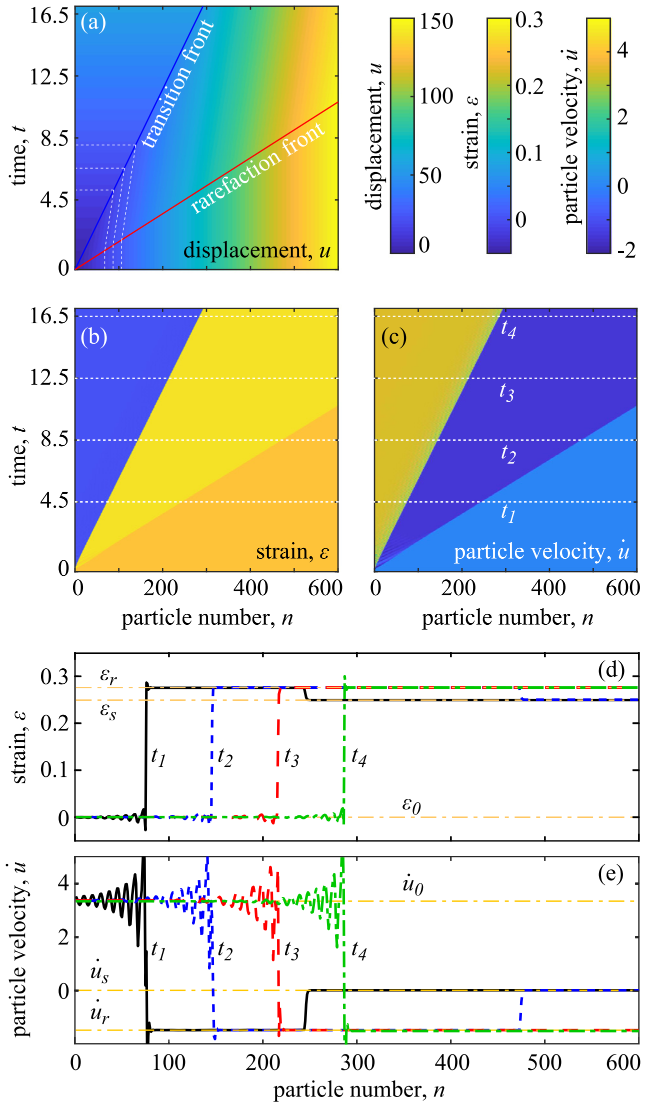

Fig. 4. Example of a propagating phase transition in a 1D bistable dissipative chain. (a) Displacement field. (b) Strain field. (c) Particle velocity field. (d–e) Strain and particle velocity profile snapshots corresponding to the four times indicated in (b–c). Material properties of the chain are specified by $\rho = 0.01$ and $\beta = 0.25$.

implies $\varepsilon_r/\varepsilon_s \to 1$. The same is observed for the dissipative limit ($\beta \gg 0$).

We next compare the theoretically obtained solutions of the transition and rarefaction wave profiles with numerical results for discrete chains. As shown in Fig. 6a, for small mass densities, the solution (30) for the *rarefaction front* matches perfectly with that obtained from discrete-chain numerical simulations. However, as the mass density increases, the differences between profiles grow in the rarefaction strain limit, owing to the low-order approximation of the interaction force (cf. Fig. 2e). The shape of the rarefaction wave depends on the mass density and viscosity. As may be expected, larger mass densities and smaller viscous damping constants result in sharper and narrower wave fronts (Figs. 6b and 6c).

Fig. 6d shows the *transition front* of kink soliton-type for three different mass densities (Eq. (35) was solved numerically for a given value of a which accounts for discreteness effect and displays a direct correlation with the oscillations behind the transition front). The transition front obtained from discrete-chain

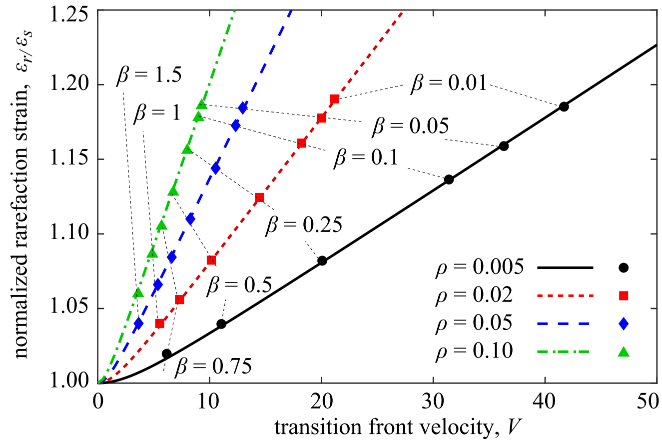

Fig. 5. Normalized rarefaction strain $\varepsilon_r/\varepsilon_s$ vs. velocity V of the transition front. Discrete-chain simulation results for various values of ρ and β are shown as markers, along with the analytical relation (37).

simulations is again superposed for comparison. These oscillations can be associated with the energy release sequencing of the stretched portion of the structure and therefore oscillate with a period of (approximately) $T = a(1+\varepsilon_s)/V$ before attenuating due to the presence of dissipation. As expected, when the mass density increases, the amplitude of oscillations increases while their wavelength decreases.

Although (33) cannot be inverted analytically for $\varepsilon(\xi)$, the relation can be plotted parametrically. As shown in Fig. 6e, we conclude from (33) that $\varepsilon(\xi) \to \varepsilon_0$ as $\xi \to -\infty$, and $\varepsilon(\xi) \to \varepsilon_r$ as $\xi \to \infty$. (These curves were produced by solving (33) twice: first by choosing $\varepsilon_{\mathrm{int}}$ arbitrarily within $\varepsilon_0 < \varepsilon_{\mathrm{int}} < \varepsilon_b$, and second from within $\varepsilon_b < \varepsilon_{\mathrm{int}} < \varepsilon_r$.)

We further explore the interface kinetics along with the energy transported and dissipated by the moving fronts (we use the same set of numerical experiments performed for Fig. 5). We compute the driving forces on the transition and rarefaction fronts, i.e., $f_{\mathrm{tr}} = D_{\mathrm{tr}}/V$ and $f_{\mathrm{rf}} = D_{\mathrm{rf}}/C$, by calculating the total dissipation potential numerically. As Fig. 7 illustrates, driving forces are in a good agreement with the numerical data. Increasing the viscous damping β or mass density ρ decreases the velocities V and C of the transition and rarefaction waves. Of course, in the diffusive limit the effects of inertia are negligible and the driving force equals $f_{\mathrm{tr}} = \psi(\varepsilon_s)$ (or $\Delta\psi = 1$), recovering the results for a grounded dissipative bistable chain [17]. Although we are interested in characterizing transition fronts of constant propagation speed, it is worth mentioning that in the weakly dissipative regime (i.e., $|m u_{,i,tt}| \sim |\beta(u_{i+1,t} - 2u_{i,t} + u_{i-1,t})/a|$) discreteness effects become significant, introducing oscillations and high-frequency twinkling modes [46,47] behind the transition front. When the effect of dissipation overtakes inertia, the velocity of the transition wave tends to decay, indicating that the energy relation ceases to apply.

The kinetics of the moving front(s) can also be interpreted by identifying the relation between the transition front velocity V and viscous damping β, which is shown in Fig. 8a, as obtained from numerical fitting. In the diffusive large-β limit, the mass density is no longer important and the transition front velocity becomes independent of the mass density ρ. At lower damping, the mass density clearly affects the front's velocity, as shown, with smaller inertia resulting in higher velocities. Apart from the effects of mass density and viscosity β, the scaling law is also related to the energy difference $\Delta\psi$ of the interaction potential between the two stable states (which, in turn, depends on the unit cell architecture in the underlying structure [22]). Figs. 8b

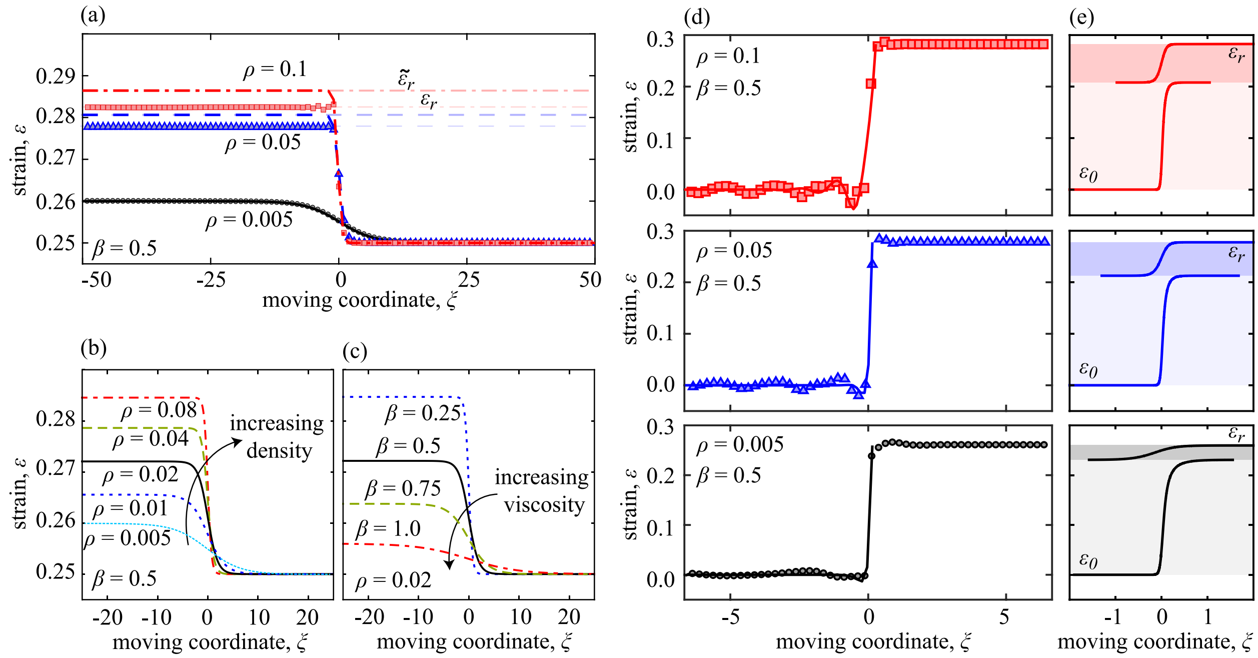

Fig. 6. Rarefaction and transition front profiles. (a) Comparison of discrete-chain numerical results (shown as markers) with the analytical solution (30) (dashed lines) obtained from the low-order approximation of the interaction potential around ε_s, for three different mass densities. (b) Effect of the mass density on the rarefaction front profile. (c) Effect of the viscosity on the rarefaction front profile. (d) Solid lines show the transition front profile which are obtained by solving (35) numerically with small discreteness effects ($a = 0.1$); numerical discrete-chain results are indicated by markers for comparison. (e) Solutions of (33) for the respective parameters shown in (d). We choose ε_{int} arbitrarily and satisfy $\varepsilon_0 < \varepsilon_{\text{int}} < \varepsilon_b$ or $\varepsilon_b < \varepsilon_{\text{int}} < \varepsilon_r$ to find ε_0 and ε_r.

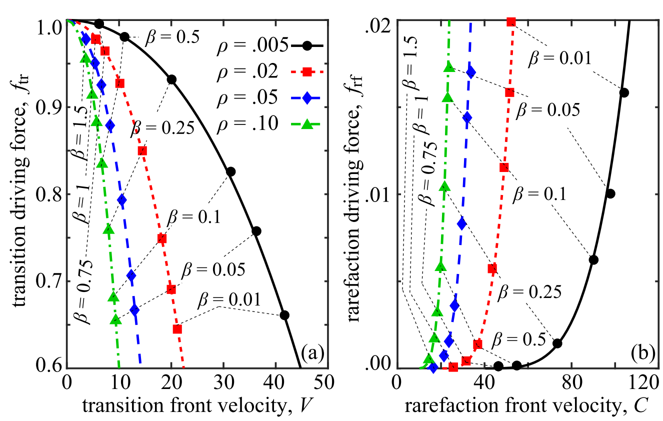

Fig. 7. Kinetics of the propagating waves. (a) Transition driving force f_{tr} vs. transition front velocity V. (b) Rarefaction driving force f_{rf} vs. rarefaction front velocity C. Results of numerical simulations for various values of ρ and β are shown as markers, analytical solutions as lines.

and 8c summarizes results for a chain of particles subjected to the various interaction potentials shown as insets (varying both the value of $\Delta\psi$ and the transformation strain ε_s while keeping the respective other constant). As expected, changing $\Delta\psi$ shifts the transition driving force proportionally. By contrast, altering the transformation strain ε_s while keeping $\Delta\psi$ = const. (which can be accomplished in experiments by altering the structural design) affects the system kinetics in a more pronounced fashion, as seen in Fig. 8c. This behavior is different from that of a grounded chain in which the energy transport relation is independent of inertia, so the energy conversion is independent of the topology of the on-site potential [17].

6. Conclusions

We have discussed substrate-free metamaterials composed of periodically repeated multistable mechanical building blocks as structural analogs of solid–solid phase transformations in materials with non-convex strain energy densities. We investigated the propagation of 1D strongly nonlinear phase transition fronts and highlighted the competition between inertial effects and dissipation (the latter stemming from viscoelastic interactions between unit cells). We showed that, while any velocity-dependent dissipation (such as friction or viscous drag) prevents stable wave motion due to the increasing tail moving as a rigid body, interaction-dependent dissipation promotes constant-speed transition waves. Akin to previous observations in phase-transforming solids, generally two propagating fronts coexist – instead of transitioning from high- to low-energy equilibrium directly, the system locally goes through an intermediate rarefaction state, thus producing both a rarefaction front (shock) and a transition front (kink). We derived solutions for the two fronts as well as the energy balance relation in the 1D chain, both a sharp-interface approximation and an exact diffuse-interface discrete chain representation. We showed the applicability of the theory to recent experiments on bistable metamaterials and presented numerical examples exploring the full design space and demonstrating the influence of inertial and dissipative damping effects. Increasing damping widens the rarefaction profile, whereas an increasing mass density increases twinkling oscillations behind the transition front. Unlike in previous studies on grounded chains, inertia here plays a central role through the kinetic energy of the moving system. Our findings highlight how the transition and rarefaction front characteristics (such as their velocities and profiles) are related to the energetics, density, and damping of the (discrete or continuous) system, and the derived relations enable the prediction and design of multistable architectures with tailored transition

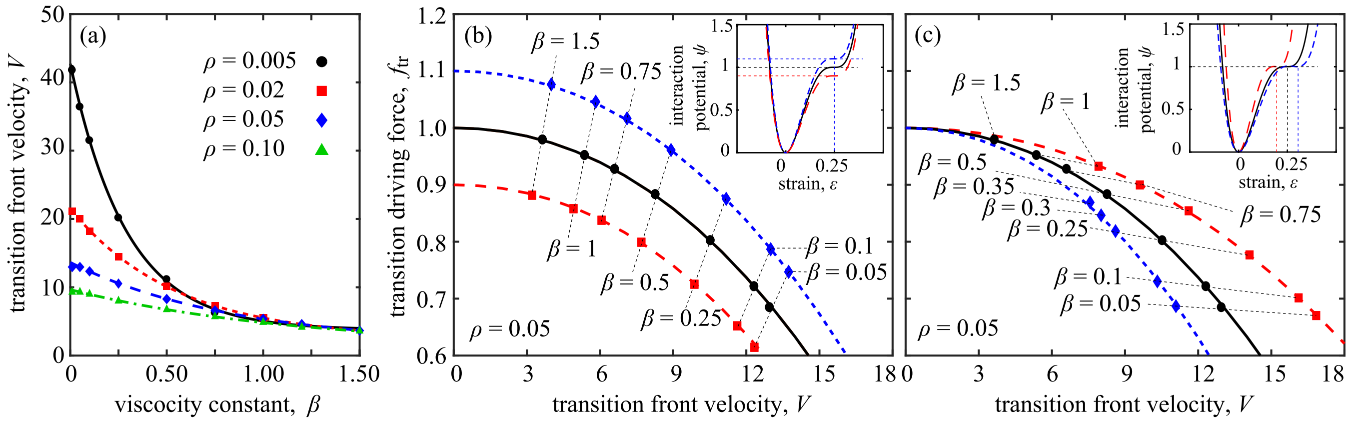

Fig. 8. Effects of the viscous damping β and non-convex interaction potential ψ on the propagating fronts. (a) Velocity V of the transition wave front vs. viscous damping β. Results of numerical simulations for various densities ρ are indicated by markers. Data are fit using an exponential relation $V = b_1 + b_2 e^{-b_3 \beta}$ with fitting parameters b_i. (b) Transition driving force f_{tr} vs. transition front velocity V for those potentials illustrated in the insets. Varying the value of the energy difference between the two stable states of the interaction potential, $\Delta\psi$ (while keeping ε_s = const.), as shown in the insets: $c_2 = 100$ (solid curve), $c_2 = 90$ (dashed curve), and $c_2 = 110$ (dotted curve). (c) Varying the transformation strain ε_s of the interaction potential while keeping $\Delta\psi$ = const.. Interaction potentials are defined by $c_2 = 166.66$, $\Delta\psi_0 = 0.006$ and $\varepsilon_s = 0.2$ (dashed curve) and by $c_2 = 80$, $\Delta\psi_0 = 0.0125$ and $\varepsilon_s = 0.3$ (dotted curve), while the solid curve is for the default parameters. Results of numerical simulations for $\rho = 0.05$ and various values of β are shown as markers, along with the theoretical solution obtained by substituting the positive root of (37) into (9).

behavior. We point out that the same general phenomena can also be observed in higher-dimensional systems (as shown by recent experiments [22]), so the theory and examples outlined here are a first step towards exploiting analogous principles in higher dimensions. Applications of such multistable architectures range from soft robotics to artificial muscles to mechanical diodes and logic.

Declaration of competing interest

The authors declare that they have no known competing financial interests or personal relationships that could have appeared to influence the work reported in this paper.

Acknowledgment

Support from the Army Research Office (ARO), USA through award W911NF-17-1-0147 is gratefully acknowledged.

Appendix A. Derivation of the energy transport relation

Starting from (11), we transform the inertial term (the first integral) into

$$\begin{aligned}\int_{-vt}^{L-vt} mv^2 u_{,\xi\xi} u_{,\xi}\,\mathrm{d}\xi &= \frac{1}{2} mv^2 \int_{-vt}^{L-vt} \frac{\partial}{\partial\xi} {u_{,\xi}}^2\,\mathrm{d}\xi \\ &= \frac{1}{2} m\dot{u}^2 \Big|_{x=0}^{x=L} = \frac{m}{2}\left(\dot{u}_+^2 - \dot{u}_-^2\right) = \frac{m}{2} [\![\dot{u}^2]\!].\end{aligned} \tag{A.1}$$

The viscous drag term becomes

$$\begin{aligned}-\int_{-vt}^{L-vt} \gamma v {u_{,\xi}}^2\,\mathrm{d}\xi &= -\int_0^L \gamma v \frac{\dot{u}^2}{v^2}\,\mathrm{d}x \\ &\approx -\frac{\gamma}{v}\left(\dot{u}_+^2 - \dot{u}_-^2\right) l(t) = -\frac{\gamma}{v} [\![\dot{u}^2]\!]\, l(t).\end{aligned} \tag{A.2}$$

To treat the interaction dissipation integral, we introduce $\eta = \xi - a$ and expand the integral into

$$\begin{aligned}&\int_{-vt}^{L-vt} \beta v \frac{u_{,\xi}(\xi + a) - u_{,\xi}(\xi)}{a} u_{,\xi}(\xi)\,\mathrm{d}\xi \\ &\quad - \int_{-vt}^{L-vt} \beta v \frac{u_{,\xi}(\xi) - u_{,\xi}(\xi - a)}{a} u_{,\xi}(\xi)\,\mathrm{d}\xi \\ &= \beta v \int_{-vt}^{L-vt} \frac{u_{,\xi}(\xi + a) - u_{,\xi}(\xi)}{a} u_{,\xi}(\xi)\,\mathrm{d}\xi \\ &\quad - \beta v \int_{-vt}^{L-vt} \frac{u_{,\eta}(\eta + a) - u_{,\eta}(\eta)}{a} u_{,\eta}(\eta + a)\,\mathrm{d}\eta.\end{aligned} \tag{A.3}$$

By changing the dummy variable η back to ξ and defining $\varepsilon(\xi) = [u(\xi + a) - u(\xi)]/a$ with $\varepsilon_{,\xi}(\xi) = [u_{,\xi}(\xi + a) - u_{,\xi}(\xi)]/a$, (A.3) becomes

$$\begin{aligned}&-\beta v a \int_{-vt}^{L-vt} \left(\frac{u_{,\xi}(\xi + a) - u_{,\xi}(\xi)}{a}\right)^2 \mathrm{d}\xi \\ &\quad = -\beta v a \int_{-vt}^{L-vt} [\varepsilon_{,\xi}(\xi)]^2\,\mathrm{d}\xi \\ &\quad = -\frac{a}{v} \int_0^L \beta \dot{\varepsilon}^2\,\mathrm{d}x = -\frac{2a}{v} \int_0^L \phi(\dot{\varepsilon})\,\mathrm{d}x.\end{aligned} \tag{A.4}$$

For a steady-state wave, we may assume $\dot{\varepsilon} = \dot{u}_{,x} = 0$ far from the wave front, so this latter integral represents the energy dissipation inside the wave front due to the dissipative particle interactions. If the wave profile is sufficiently smooth and the wavefront sufficiently wide, then

$$\int_0^L \phi(\dot{\varepsilon})\,\mathrm{d}x \approx \sum_{i=1}^{N-1} \phi(\dot{\varepsilon}_i) a = \frac{1}{2} D_{\mathrm{discr}} \tag{A.5}$$

represents the total dissipation potential due to the viscous particle interactions (D_{discr} denoting the total dissipation).

Analogously, the non-convex interaction potential term becomes

$$
\begin{aligned}
&-\int_{-vt}^{L-vt}\left[\psi'\left(\frac{u(\xi+a)-u(\xi)}{a}\right)\right.\\
&\left.-\psi'\left(\frac{u(\xi)-u(\xi-a)}{a}\right)\right]u_{,\xi}\,\mathrm{d}\xi\\
&=-\int_{-vt}^{L-vt}\psi'\Big(\frac{u(\xi+a)-u(\xi)}{a}\Big)u_{,\xi}(\xi)d\xi\\
&+\int_{-vt}^{L-vt}\psi'\Big(\frac{u(\eta+a)-u(\eta)}{a}\Big)u_{,\eta}(\eta+a)d\eta\\
&=-\int_{-vt}^{L-vt}\psi'\left(\frac{u(\xi+a)-u(\xi)}{a}\right)(u_{,\xi}(\xi)-u_{,\xi}(\xi+a))\mathrm{d}\xi.
\end{aligned}
\tag{A.6}
$$

When the transition wave switches the state of the system from $\lim_{\xi\to+\infty}\psi(\varepsilon(\xi))$ to $\lim_{\xi\to-\infty}\psi(\varepsilon(\xi))$, the interaction integral contribution becomes

$$
\begin{aligned}
&-\int_{-vt}^{L-vt}\Big[\psi'\Big(\frac{u(\xi+a)-u(\xi)}{a}\Big)-\psi'\Big(\frac{u(\xi)-u(\xi-a)}{a}\Big)\Big]u_{,\xi}d\xi\\
&=a\int_{\varepsilon_-}^{\varepsilon_+}\psi'(\varepsilon)\mathrm{d}\varepsilon=a\left[\psi(\varepsilon_+)-\psi(\varepsilon_-)\right]=a\,[\![\psi]\!].
\end{aligned}
\tag{A.7}
$$

Appendix B. Energy exchange in a continuous body

We assume $v > 0$ and substitute a solution of the form $u(x,t)=\hat{u}(\xi)+\varepsilon_{int}x$ into (7), multiply by $u_{,\xi}$ and integrating over a body of length L. The resulting inertial, viscous drag and friction terms are analogous to the discrete case. For the viscous particle interactions, the integral now becomes

$$
\beta v\int_{-vt}^{L-vt}u_{,\xi\xi\xi}u_{,\xi}\,\mathrm{d}\xi=-\frac{2}{v}\int_0^L\phi(\dot{\varepsilon})\mathrm{d}x=-\frac{D}{v}
\tag{B.1}
$$

with the total (exact) dissipation $D>0$. Similarly, we expand the interaction integral, accounting for $\psi'(u_{,\xi})=0$ at $\xi=-vt$ and $\xi=L-vt$, which gives

$$
-\int_{-vt}^{L-vt}\psi''(u_{,\xi})u_{,\xi\xi}u_{,\xi}\,\mathrm{d}\xi=\int_0^L\psi'(\varepsilon)\varepsilon_{,x}\mathrm{d}x=[\![\psi(\varepsilon)]\!].
\tag{B.2}
$$

We thus arrive at the continuous version of (16):

$$
\frac{\rho}{2}[\![\dot{u}^2]\!]-(2\eta\langle\dot{u}\rangle+\tau)\frac{[\![\dot{u}]\!]}{v}l(t)-\frac{D}{v}+[\![\psi]\!]=0.
\tag{B.3}
$$

We again conclude that the constant-speed, steady-state solution only exists if $\eta=0$ and $\tau=0$ (i.e., in the absence of friction and drag, if $[\![\psi]\!]=$ const. throughout the body). Consequently, we recover (17) and (19) with the exception of the discrete dissipation D_{discr} replaced by the exact continuous counterpart D. Obviously, in case of smooth solutions with a wide transition front, $D_{\mathrm{discr}}\approx D$ so the discrete and continuous forms coincide.

Appendix C. Effect of the impact velocity

Fig. C.9 illustrates the transition and rarefaction front velocities (V and C, respectively) for different combinations of mass and viscosity values as well as for different impact velocity v_{imp}. Below a cut-off impact velocity, only an elastic wave exists with speed $\sqrt{\psi''(\varepsilon_s)/\rho}$, whereas above the cut-off two fronts with distinct velocities propagate through the chain. Those do not change when varying the impact velocity (above the cut-off). The cut-off velocity is directly related to the Peierls–Nabarro stress in the system, imposing the amount of force required to overcome the energy barrier to establish a transition wave [48,49].

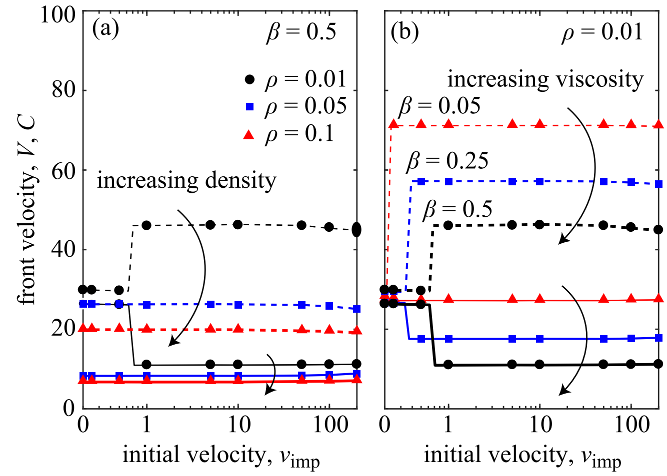

Fig. C.9. Effect of the impact velocity v_{imp} (defined as the initial velocity of the leftmost particle at $t=0$) on the velocity of the transition front, V (solid lines), and of the rarefaction front, C (dashed lines) in a discrete chain. (a) Effect of the mass. (c) Effect of the viscous damping.

References

[1] J. Frenkel, T. Kontorova, On the theory of plastic deformation and twinning, Phys. Z. Sowjetunion 13 (1938) 1.
[2] A. Bishop, W. Lewis, A theory of intrinsic coercivity in narrow magnetic domain wall materials, J. Phys. C: Solid State Phys. 12 (18) (1979) 3811.
[3] M. Peyrard, A.R. Bishop, Statistical mechanics of a nonlinear model for DNA denaturation, Phys. Rev. Lett. 62 (23) (1989) 2755.
[4] P. Giri, K. Choudhary, A. Dey, A. Biswas, A. Ghosal, A. Bandyopadhyay, Discrete energy levels of bright solitons in lithium niobate ferroelectrics, Phys. Rev. B 86 (18) (2012) 184101.
[5] L. Truskinovsky, A. Vainchtein, Kinetics of martensitic phase transitions: lattice model, SIAM J. Appl. Math. 66 (2) (2005) 533–553.
[6] E. Trofimov, A. Vainchtein, Shocks versus kinks in a discrete model of displacive phase transitions, Contin. Mech. Thermodyn. 22 (5) (2010) 317–344.
[7] D. Angeli, J.E. Ferrell, E.D. Sontag, Detection of multistability, bifurcations, and hysteresis in a large class of biological positive-feedback systems, Proc. Natl. Acad. Sci. 101 (7) (2004) 1822–1827.
[8] H. Rotermund, S. Jakubith, A. Von Oertzen, G. Ertl, Solitons in a surface reaction, Phys. Rev. Lett. 66 (23) (1991) 3083.
[9] M.J. Ablowitz, P.A. Clarkson, Solitons, Nonlinear Evolution Equations and Inverse Scattering, Vol. 149, Cambridge university press, 1991.
[10] M. Hussein, R. Khajehtourian, Nonlinear Bloch waves and balance between hardening and softening dispersion, Proc. R. Soc. A: Math. Phys. Eng. Sci. 474 (2217) (2018) 20180173.
[11] R. Khajehtourian, M. Hussein, Nonlinear dispersion relation predicts harmonic generation in wave motion, 2019, arXiv preprint arXiv:1905.02523.
[12] N. Akhmediev, A. Ankiewicz, Dissipative solitons in the complex Ginzburg-Landau and Swift-Hohenberg equations, in: Dissipative Solitons, Springer, 2005.
[13] R.D. James, The propagation of phase boundaries in elastic bars, Arch. Ration. Mech. Anal. 73 (2) (1980) 125–158.
[14] L. Truskinovsky, Nucleation and growth in elastodynamics, in: Dynamics of Crystal Surfaces and Interfaces, Springer, 2002, pp. 185–197.
[15] A.C. Scott, A nonlinear Klein-Gordon equation, Amer. J. Phys. 37 (1) (1969) 52–61.
[16] N. Nadkarni, C. Daraio, D.M. Kochmann, Dynamics of periodic mechanical structures containing bistable elastic elements: From elastic to solitary wave propagation, Phys. Rev. E 90 (2) (2014) 023204.
[17] N. Nadkarni, C. Daraio, R. Abeyaratne, D.M. Kochmann, Universal energy transport law for dissipative and diffusive phase transitions, Phys. Rev. B 93 (10) (2016) 104109.
[18] N. Nadkarni, A.F. Arrieta, C. Chong, D.M. Kochmann, C. Daraio, Unidirectional transition waves in bistable lattices, Phys. Rev. Lett. 116 (24) (2016) 244501.
[19] J.R. Raney, N. Nadkarni, C. Daraio, D.M. Kochmann, J.A. Lewis, K. Bertoldi, Stable propagation of mechanical signals in soft media using stored elastic energy, Proc. Natl. Acad. Sci. 113 (35) (2016) 9722–9727.

[20] M.J. Frazier, D.M. Kochmann, Atomimetic mechanical structures with nonlinear topological domain evolution kinetics, Adv. Mater. 29 (19) (2017) 1605800.
[21] O.M. Braun, Y.S. Kivshar, Nonlinear dynamics of the Frenkel–Kontorova model, Phys. Rep. 306 (1–2) (1998) 1–108.
[22] L. Jin, R. Khajehtourian, J. Mueller, A. Rafsanjani, V. Tournat, K. Bertoldi, D.M. Kochmann, Guided transition waves in multistable mechanical metamaterials, Proc. Natl. Acad. Sci. 117 (5) (2020) pnas.1913228117.
[23] L. Manevitch, V. Smirnov, Propagation of exothermic reactions in condensed matter, Phys. Lett. A 165 (5–6) (1992) 427–431.
[24] L.I. Manevich, A.V. Savin, V.V. Smirnov, S.N. Volkov, Solitons in nondegenerate bistable systems, Phys.-Usp. 37 (9) (1994) 859.
[25] S. Katz, S. Givli, Solitary waves in a bistable lattice, Extreme Mech. Lett. 22 (2018) 106–111.
[26] L. Slepyan, A. Cherkaev, E. Cherkaev, Transition waves in bistable structures. II. Analytical solution: wave speed and energy dissipation, J. Mech. Phys. Solids 53 (2) (2005) 407–436.
[27] I. Markov, A. Milchev, Theory of epitaxy in a Frank-van der Merwe model with anharmonic interactions, Thin Solid Films 126 (1–2) (1985) 83–93.
[28] O. Braun, B. Hu, A. Zeltser, Driven kink in the Frenkel-Kontorova model, Phys. Rev. E 62 (3) (2000) 4235.
[29] S. Watanabe, H.S. van der Zant, S.H. Strogatz, T.P. Orlando, Dynamics of circular arrays of Josephson junctions and the discrete sine-Gordon equation, Physica D 97 (4) (1996) 429–470.
[30] L. Truskinovsky, A. Vainchtein, Dynamics of martensitic phase boundaries: discreteness, dissipation and inertia, Contin. Mech. Thermodyn. 20 (2) (2008) 97–122.
[31] A. Vainchtein, The role of spinodal region in the kinetics of lattice phase transitions, J. Mech. Phys. Solids 58 (2) (2010) 227–240.
[32] B. Deng, P. Wang, V. Tournat, K. Bertoldi, Nonlinear transition waves in free-standing bistable chains, J. Mech. Phys. Solids (2019) 103661.
[33] J. Christian, G. Olson, M. Cohen, Classification of displacive transformations: What is a martensitic transformation? J. Phys. IV 5 (C8) (1995) C8–3.
[34] J. Christian, S. Mahajan, Deformation twinning, Prog. Mater. Sci. 39 (1–2) (1995) 1–157.
[35] K. Bhattacharya, Microstructure of Martensite, Oxford University Press, Oxford, UK, 2003.
[36] R. Dhote, H. Gomez, R. Melnik, J. Zu, 3D coupled thermo-mechanical phase-field modeling of shape memory alloy dynamics via isogeometric analysis, Comput. Struct. 154 (2015) 48–58.
[37] R. Abeyaratne, J.K. Knowles, Kinetic relations and the propagation of phase boundaries in solids, Arch. Ration. Mech. Anal. 114 (2) (1991) 119–154.
[38] O. Penrose, P.C. Fife, Thermodynamically consistent models of phase-field type for the kinetic of phase transitions, Physica D 43 (1) (1990) 44–62.
[39] L. Truskinovsky, Kinks versus shocks, in: Shock Induced Transitions and Phase Structures in General Media, Springer, 1993, pp. 185–229.
[40] V. Agrawal, K. Bhattacharya, Shock wave propagation through a model one dimensional heterogeneous medium, Int. J. Solids Struct. 51 (21–22) (2014) 3604–3618.
[41] L.D. Landau, On the theory of phase transitions (in Russian), Zh. Eksp. Teor. Fiz. 7 (1937) 19–32.
[42] S.-C. Ngan, L. Truskinovsky, Thermo-elastic aspects of dynamic nucleation, J. Mech. Phys. Solids 50 (6) (2002) 1193–1229.
[43] V.L. Ginzburg, L.D. Landau, English translation in: L. D. Landau, collected papers (Oxford: Pergamon press, 1965) p. 546, Zh. Eksp. Teor. Fiz. 20 (1950) 1064.
[44] A. Devonshire, XCVI. Theory of barium titanate, Phil. Mag. Ser. 7 40 (309) (1949) 1040–1063.
[45] J.A. Wattis, Approximations to solitary waves on lattices. II. Quasi-continuum methods for fast and slow waves, J. Phys. A: Math. Gen. 26 (5) (1993) 1193.
[46] A.M. Balk, A.V. Cherkaev, L.I. Slepyan, Dynamics of chains with non-monotone stress-strain relations. II. Nonlinear waves and waves of phase transition, J. Mech. Phys. Solids 49 (2001) 149–171.
[47] B.F. Feeny, A.R. Diaz, Twinkling phenomena in snap-through oscillators, J. Vib. Acoust. 132 (6) (2010).
[48] R. Peierls, The size of a dislocation, Proc. Phys. Soc. 52 (1) (1940) 34.
[49] F. Nabarro, Dislocations in a simple cubic lattice, Proc. Phys. Soc. 59 (2) (1947) 256.